energies

Article

A Fault Identification Method for Metal Oxide Arresters Combining Suppression of Environmental Temperature and Humidity Interference with a Stacked Autoencoder

Shengwen Shu [1,*], Xiaoyao Zhang [1], Guobin Wang [2], Jinglan Zeng [2] and Ying Ruan [2]

1 School of Electrical Engineering and Automation, Fuzhou University, Fuzhou 350108, China; 220127127@fzu.edu.cn
2 Electric Power Research Institute, State Grid Fujian Electric Power Co., Ltd., Fuzhou 350007, China; 18350130493@163.com (G.W.); m15280403187@163.com (J.Z.); djry132@sina.com (Y.R.)
* Correspondence: shushengwen@fzu.edu.cn

Abstract: Most existing methods aiming to solve the fault identification problem of metal oxide arresters (MOAs) are limited by strong subjectivity in judgment, the significant impact of environmental temperature and humidity on the online monitoring of the resistance current, and poor generalization ability. Therefore, in this article, we propose an MOA fault identification method that combines suppressing environmental temperature and humidity interference with a stacked autoencoder (SAE). Firstly, a functional relationship model between resistance current and environmental temperature and humidity is established. Then, a temperature and humidity interference suppression method based on weighted nonlinear surface modeling is proposed to normalize the resistance current to the same reference temperature and humidity conditions. Finally, an MOA fault identification method combining the suppression of environmental temperature and humidity interference with an SAE is proposed. Furthermore, a comprehensive comparison is conducted on the recall, accuracy, F_1-score, and average accuracy of support vector machine, random forest, logistic regression, and SAE classification algorithms in three different scenarios to demonstrate the effectiveness of the proposed method. The results indicate that environmental temperature and humidity interference suppression for resistive current prior to MOA fault classification significantly reduce the number of false alarms. Compared with other methods, the MOA fault identification method, which combines environmental temperature and humidity interference suppression with an SAE, has the highest average accuracy of 99.7%.

Keywords: metal oxide arrester (MOA); fault identification; environmental temperature and humidity; interference suppression; stacked autoencoder (SAE)

Citation: Shu, S.; Zhang, X.; Wang, G.; Zeng, J.; Ruan, Y. A Fault Identification Method for Metal Oxide Arresters Combining Suppression of Environmental Temperature and Humidity Interference with a Stacked Autoencoder. *Energies* **2023**, *16*, 8033. https://doi.org/10.3390/en16248033

Academic Editor: Andrea Mariscotti

Received: 1 November 2023
Revised: 29 November 2023
Accepted: 8 December 2023
Published: 12 December 2023

1. Introduction

The metal oxide arrester (MOA) is a significant component of the surge protection device in a power supply system. However, in the long-term operation process, the insulation performance of the MOA will reduce due to varistor aging, moisture, current surge, and other factors that threaten the safe operation of the power supply system. As a result, it is necessary to monitor the operating status of the MOA in a timely fashion and send fault alarms to improve the reliability of the power system [1–3].

At present, the online monitoring methods for MOAs mainly include full current, resistive current, harmonic current, and infrared thermal imaging methods. In [4], an inverse-distance-weighted improved *K*-nearest neighbor algorithm was adopted to determine the resistive current for defect diagnosis of an MOA. In [5], a three-phase segmented arrester resistive network circuit model was established to filter out the capacitive component of the full current. In [6], the harmonic analysis method was used for the online monitoring of an MOA. In [7–9], the infrared thermal imaging method was adopted to monitor the heating status of an MOA. Both the full-current method and the infrared thermal imaging method are susceptible to the on-site weather environment, which can cause many false alarms. Due to its simplicity, convenience, and sensitivity to reflecting the state of the MOA, the resistive current method has been widely used in monitoring the operational status of MOAs [10].

To solve the MOA fault identification problem, various methods have been studied, mainly including expert knowledge [11–16], artificial intelligence algorithms [17,18], artificial neural networks (ANNs) [19,20], and deep learning [21–23]. In [15,16], a fuzzy evaluation method for the MOA operation state based on information fusion was proposed. In [18], an MOA degradation monitoring method was proposed based on the genetic algorithm (GA). In [19,20], an ANN was utilized to identify the features of MOA faults. However, the ANN still possesses certain limitations, including prolonged training time, susceptibility to overfitting, and unsatisfactory generalization ability [24,25]. Compared to ANNs, deep learning performs layer-by-layer feature transformations to shift the feature representation of samples from the original space to a new feature space, making classification or prediction easier and being better suited to fault detection in electrical systems [26–28]. In [21–23], a support vector machine (SVM) was employed to enhance the detection accuracy of MOA faults.

In addition, the online monitoring feature quantity of an MOA is easily affected by the environment [29–33]. In [29], a method for eliminating interference due to the resistive current of an MOA based on adaptive variational mode decomposition and adaptive singular value decomposition was proposed. Mathematical morphological filters were used in [34] to denoise the on-site monitoring signal of an MOA leakage current with a strong interference background. In [35], on-line monitoring of the full current and temperature and humidity variations of surge arresters was carried out, and it was concluded that these variations have some correlation in field tests. In [36,37], the trend of the leakage current of an MOA changing with temperature and humidity was analyzed. In [38], the influence of temperature on the characteristic parameters of an MOA was studied and a correction method was proposed, but the influence of environmental humidity was not considered. In [39], the impact of environmental temperature and humidity was considered during online monitoring of an MOA, and BP neural networks were used to correct MOA parameters by establishing the relationship between these parameters and temperature and humidity. However, the Levenberg–Marquardt training algorithm used in [39] was prone to falling into local optima. In [40], Bayesian neural network models were used to reduce the effect of meteorological factors on the full current, but MOA fault classification was not implemented.

In existing studies, some correction methods for the MOA resistive current considering the effects of environmental temperature or humidity have been proposed, but a universal correction method considering the effects of both environmental temperature and humidity is lacking. Furthermore, some MOA fault identification models based on deep learning have been established to overcome the shortcomings of a long training time, easy overfitting, and poor generalization ability. However, in these deep learning models, the suppression of environmental temperature and humidity has rarely been carried out.

To overcome the above shortcomings of the existing methods, we propose an MOA fault identification method that combines the suppression of environmental temperature and humidity interference with a stacked autoencoder (SAE). The main contributions of this paper are as follows:

(1) A functional relationship model between resistive current and environmental temperature and humidity is established to mitigate the impact of environmental temperature and humidity on the resistive current of an MOA. A method for suppressing environmental temperature and humidity interference using weighted nonlinear surface modeling is proposed. This method normalizes the resistive current to the reference temperature and humidity, resulting in a reduction in environmental interference with the resistive current.

(2) An MOA fault identification method combining the suppression of environmental temperature and humidity interference with a stacking automatic encoder is proposed. Firstly, the MOA resistive current is suppressed by environmental temperature and humidity interference, and then the SAE classification algorithm is used to classify the suppressed resistive current, thereby achieving MOA fault identification.
(3) The effectiveness of the MOA fault recognition method combining suppression of environmental temperature and humidity interference with a stacking automatic encoder is verified by comparison with several commonly used classification algorithms under three conditions: not considering environmental temperature and humidity, feature fusion of environmental temperature and humidity with resistive current, and suppression of environmental temperature and humidity interference.

The remainder of the article is organized as follows. Section 2 describes the MOA fault identification method, which combines suppression of environmental temperature and humidity interference with an SAE. In Section 3, the MOA fault identification results are provided. Finally, the conclusions are given in Section 4.

2. Methods

To mitigate the effects of humidity and temperature on the MOA resistive current, it is essential to construct a precise functional model that details the relationship between environmental temperature, humidity, and resistive current. In this section, we put forward a method for normalizing the resistive current to the base temperature and humidity, thereby reducing the impact of environmental temperature and humidity on the resistive current. Then, the resistive current after the suppression of environmental temperature and humidity interference is classified by the SAE classification algorithm to achieve MOA fault classification.

2.1. General Framework

The resistive current of an MOA is susceptible to the influence of ambient temperature and humidity, and it is crucial to effectively suppress the interference of ambient temperature and humidity on the MOA resistive current. Figure 1 shows the original data in respect of the MOA resistive current, ambient temperature, and humidity during 3000 continuous hours. Figure 2 shows the general framework of the MOA fault identification method combining ambient temperature and humidity interference suppression and an SAE that is proposed in this paper.

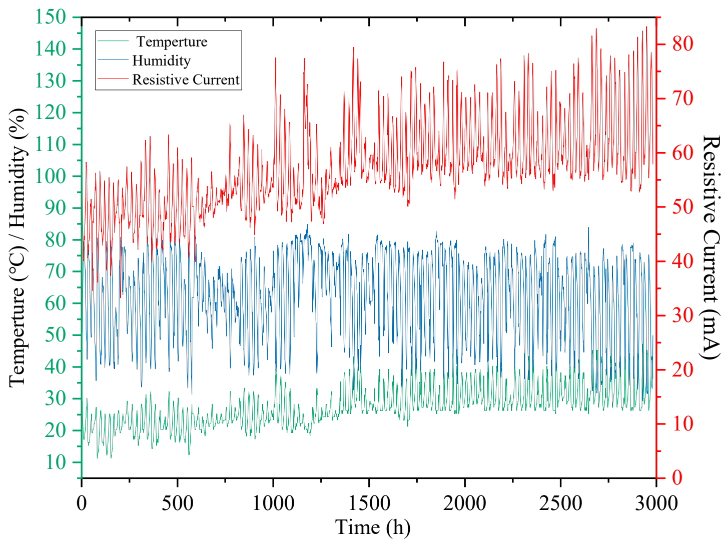

Figure 1. Original data in respect of MOA resistive current, environmental temperature, and humidity.

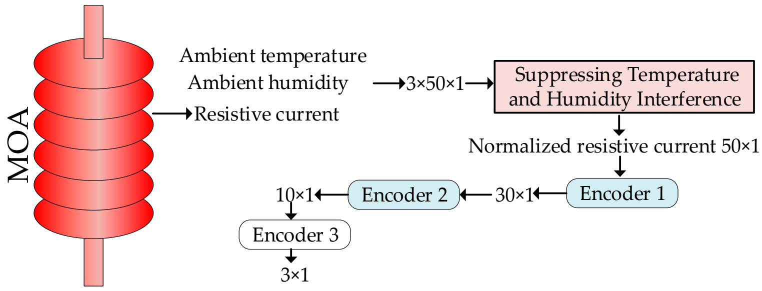

Figure 2. Framework diagram of the MOA fault identification method combining temperature and humidity interference suppression with SAE.

2.2. A Method of Environmental Temperature and Humidity Interference Suppression

Considering that the resistive current of an MOA has linear and non-linear relationships with environmental temperature and humidity at low and high environmental temperature and humidity, a combination of linear and nonlinear models is adopted in this paper to fit the resistive current and environmental temperature and humidity. The flowchart of the proposed method is shown in Algorithm 1.

Figure 3 shows the structure of the SAE classification algorithm. Its operating principles are as follows. After the autoencoder's data training, the output x_i network encoder is used as an input for the subsequent autoencoder. Eventually, the coding components of several autoencoders are cascaded. This layer-by-layer training method can reduce the computational force requirements, prevent gradient dissipation, and achieve rapid convergence of results in subsequent training, which is a method of achieving data dimensionality reduction through unsupervised training. The network can be used as an algorithm for transfer learning, sharing weights in different application scenarios, eliminating the process of pre-training, and reducing the amount of calculation.

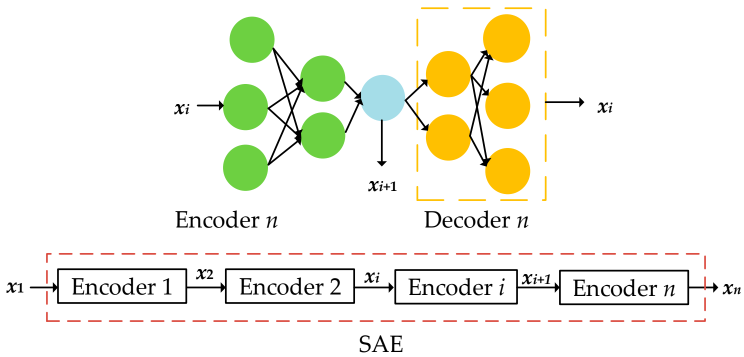

Figure 3. Stacked self-encoding structure.

In this process, the input of each layer of the network is batch-normalized, which speeds up the rate of convergence of the model. A dropout layer, having a parameter of 0.3, is suitably incorporated into every layer. Some neurons are randomly discarded in the iterative process, which can improve network robustness, network generalization ability, and prevent overfitting.

Algorithm 1 Temperature and humidity interference suppression algorithm.

Model: $I_r(b,t,h) = b_0 + b_1 t + b_2 h + b_3 th + b_4 e^{b_5 t} + b_6 e^{b_7 h}$
Require: Input N MOA original data ($\boldsymbol{I_r}$, $\boldsymbol{t}$, $\boldsymbol{h}$) and initial value $\boldsymbol{b}^{(0)} = [b_0{}^{(0)}, b_1{}^{(0)}, \ldots, b_7{}^{(0)}]^{\mathrm{T}}$
for $i \leftarrow 0$ to K **do**
for $j \leftarrow 1$ to N **do**
Calculate the error between the fitted value and the truth value of I_r

$$\Delta I_{rj}^{(i)} = b_0{}^{(i)} + b_1{}^{(i)} t_j + b_2{}^{(i)} h_j + b_3{}^{(i)} t_j h_j + b_4{}^{(i)} e^{b_5{}^{(i)} t_j} + b_6 e^{b_7{}^{(i)} h_j} - I_{r0j}$$

if $\max\left\{\Delta I_{r1}^{(i)}, \Delta I_{r2}^{(i)}, \cdots, \Delta I_{rN}^{(i)}\right\} \geq \varepsilon$ **then**

$$u_j^{(i)} = 0.6745 \frac{\Delta I_{rj}^{(i)}}{Median\left|\Delta I_{rj}^{(i)} - Median(\Delta I_{r1}^{(i)}, \cdots, \Delta I_{rN}^{(i)})\right|}$$

$$q_j^{(i)} = \begin{cases} 1, & \left|u_j^{(i)}\right| \leq 1.345 \\ 1.345/\left|u_j^{(i)}\right|, & \left|u_j^{(i)}\right| > 1.345 \end{cases}$$

$$\boldsymbol{q}^{(i)} = diag(q_1^{(i)}, q_2^{(i)}, \cdots, q_N^{(i)}) = \begin{bmatrix} q_1^{(i)} & 0 & \cdots & 0 \\ 0 & q_2^{(i)} & \cdots & 0 \\ \cdots & \cdots & \cdots & \cdots \\ 0 & 0 & \cdots & q_N^{(i)} \end{bmatrix}$$

$$\boldsymbol{G}^{(i)} = \begin{bmatrix} G_1^{(i)}(b_0^{(i)}, b_1^{(i)}, \ldots, b_7^{(i)}) \\ G_2^{(i)}(b_0^{(i)}, b_1^{(i)}, \ldots, b_7^{(i)}) \\ \cdots \\ G_N^{(i)}(b_0^{(i)}, b_1^{(i)}, \ldots, b_7^{(i)}) \end{bmatrix}$$

$$\Delta \boldsymbol{J}^{(i)} = \begin{bmatrix} \frac{\partial G_1^{(i)}}{\partial b_0} & \frac{\partial G_1^{(i)}}{\partial b_1} & \cdots & \frac{\partial G_1^{(i)}}{\partial b_7} \\ \frac{\partial G_2^{(i)}}{\partial b_0} & \frac{\partial G_2^{(i)}}{\partial b_1} & \cdots & \frac{\partial G_2^{(i)}}{\partial b_7} \\ \cdots & \cdots & \cdots & \cdots \\ \frac{\partial G_N^{(i)}}{\partial b_0} & \frac{\partial G_N^{(i)}}{\partial b_1} & \cdots & \frac{\partial G_N^{(i)}}{\partial b_7} \end{bmatrix}$$

$$\Delta \boldsymbol{b}^{(i+1)} = -\left((\Delta \boldsymbol{J}^{(i)})^{\mathrm{T}} \boldsymbol{q}^{(i)} \Delta \boldsymbol{J}^{(i)}\right)^{-1} (\Delta \boldsymbol{J}^{(i)})^{\mathrm{T}} \boldsymbol{q}^{(i)} \boldsymbol{G}^{(i)}$$

Updated $\boldsymbol{b}^{(i)}$

$$\boldsymbol{b}^{(i+1)} = \boldsymbol{b}^{(i)} + \Delta \boldsymbol{b}^{(i)}$$

else
$i = k$
Obtain $\boldsymbol{b}^{(k)} = [b_0{}^{(k)}, b_1{}^{(k)}, \ldots, b_7{}^{(k)}]$

$$\text{Solve } \boldsymbol{G}^{(k)} = \begin{bmatrix} G_1^{(k)}(b_0^{(k)}, b_1^{(k)}, \ldots, b_7^{(k)}) \\ G_2^{(k)}(b_0^{(k)}, b_1^{(k)}, \ldots, b_7^{(k)}) \\ \cdots \\ G_N^{(k)}(b_0^{(k)}, b_1^{(k)}, \ldots, b_7^{(k)}) \end{bmatrix} = 0$$

i.e., Solve $G_j(t_j, h_j, I'_{rj}) = 0$
Obtain I'_{rj}
return I'_{rj}.

2.3. SAE

The SAE algorithm is presented in Algorithm 2.

Algorithm 2 SAE.

Require: Input the data $\boldsymbol{x}_1$ to be classified
$\boldsymbol{x}_2 = f_e(\boldsymbol{W}_1 \boldsymbol{x}_1 + \boldsymbol{a}_1)$
obtain $\boldsymbol{x}_2$ with a vector length of 30
$\boldsymbol{x}_3 = f_e(\boldsymbol{W}_1 \boldsymbol{x}_2 + \boldsymbol{a}_1)$
obtain $\boldsymbol{x}_3$ with a vector length of 3
$\boldsymbol{y}_1 = f_d(\boldsymbol{W}_2 \boldsymbol{x}_3 + \boldsymbol{a}_2)$
obtain $\boldsymbol{y}_2$ with a vector length of 30
$\boldsymbol{x}_1 = f_d(\boldsymbol{W}_2 \boldsymbol{y}_1 + \boldsymbol{a}_2)$
Output: Numbers representing categories.

2.4. Comparison Algorithm: Feature Fusion

To verify the effectiveness of the algorithm proposed in this paper, we use the feature fusion algorithm as a comparison algorithm, considering the effect of ambient temperature and humidity on the MOA resistive current. Firstly, the ambient temperature and humidity and the resistive current are dimensionally reduced, and then the reduced data are fused into a column; finally, the fused data are classified. The whole network utilizes an "Adam" optimizer in the output layer with a "Softmax" activation function and a "Categorical_crossentropy" loss function, which generates outputs in three dimensions. The activation function of the other layers is "Relu", and the loss function is "MSE". The network framework is shown in Figure 4.

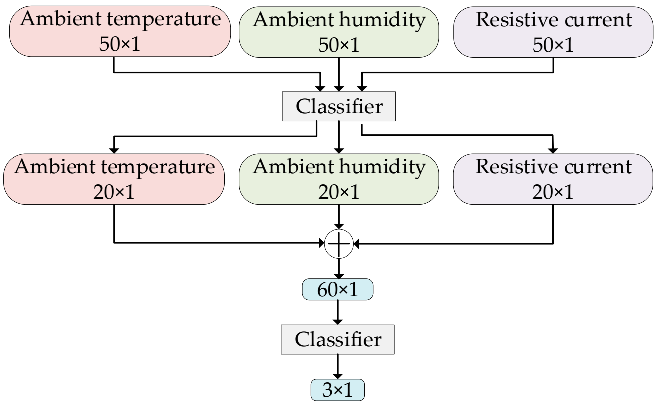

Figure 4. Feature fusion network framework.

3. Results

In this section, taking 110 kV MOA resistive current data from a certain province in China as an example, the effectiveness of the MOA fault identification method combining temperature and humidity interference suppression with an SAE is verified. Firstly, the MOA data samples used in this article are introduced and analyzed statistically. Then, the effectiveness of the method for suppressing temperature and humidity based on weighted nonlinear surface modeling is discussed. Finally, the proposed MOA fault identification method is compared with other classification algorithms by means of several model evaluation indicators.

3.1. Data Samples

In this paper, a total of 15,800, 4500, and 3400 original MOA data points relating to the normal state, an MOA fault, and monitoring device failure are used, respectively. Figures 5–7 show the original data in respect of MOA resistive current and environmental temperature and humidity during a continuous 500 h period under normal conditions, MOA fault, and monitoring device failure, respectively. Also, the frequency distribution histograms of all of the data used in respect of resistive current, environmental temperature, and humidity of the MOA under different conditions are illustrated in Figures 5–7.

It can be seen from Figures 5–7 that the resistive current ranges from 20 mA to 80 mA during normal MOA states, which are lower compared to those for MOA faults and monitoring device failure. Furthermore, the resistive current under the condition of MOA monitoring device failure fluctuates more significantly than the other two conditions. Whether under normal operating conditions, the MOA fault, or the monitoring device failure, the environmental temperature and humidity span wide ranges, which are approximately 0–40 °C and 10–98%, respectively. In addition, the MOA resistive current changes with the fluctuations in environmental temperature and humidity. Therefore, the results are replicable and can be generalized to different scenarios and conditions.

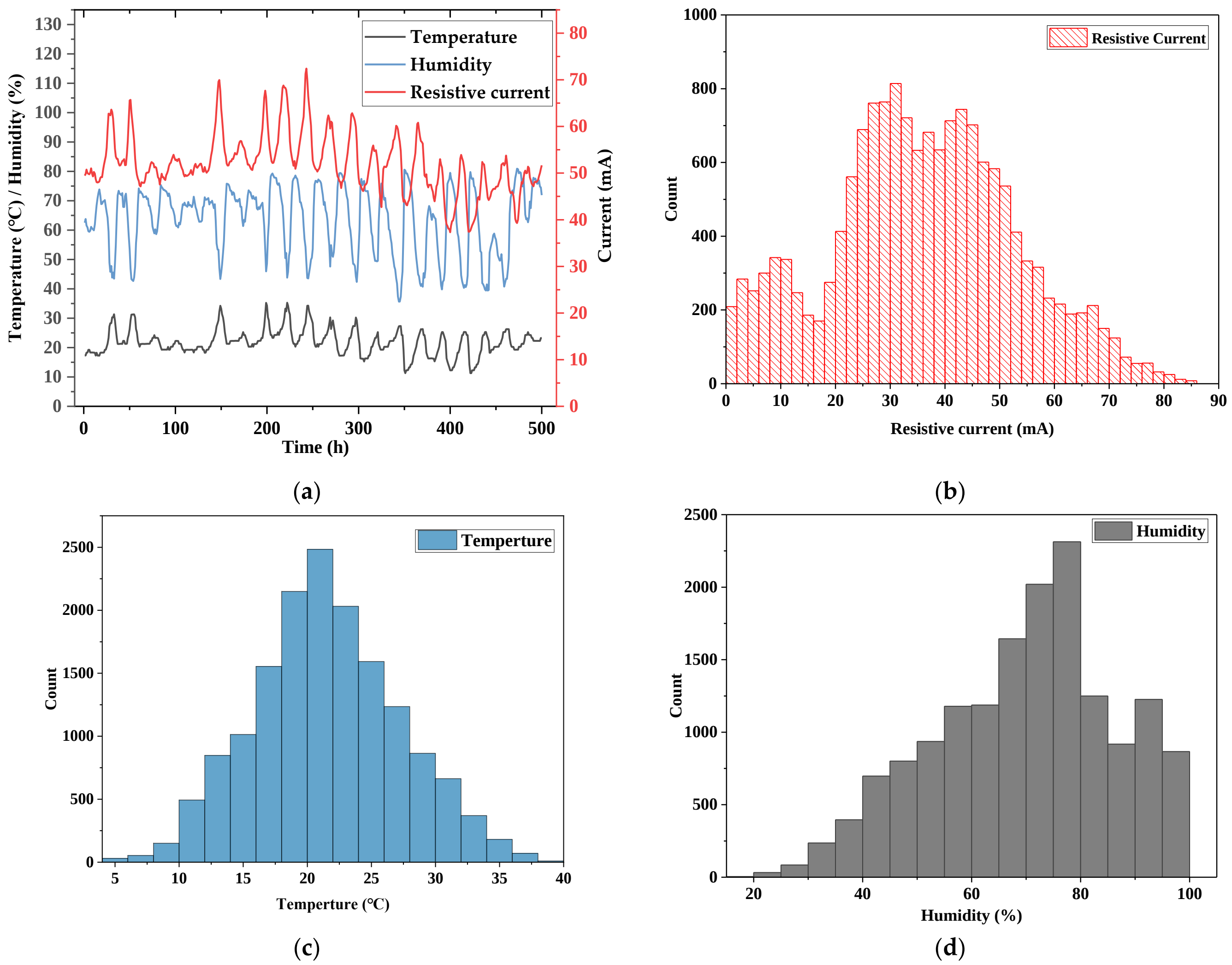

Figure 5. Original data and histograms of the frequency distribution under a normal MOA state. (**a**) Original data in respect of resistive current and environmental temperature and humidity; (**b**) histogram of the frequency distribution of the MOA resistive current; (**c**) histogram of the frequency distribution of environmental temperature; (**d**) histogram of the frequency distribution of environmental humidity under normal conditions.

3.2. Model Evaluation Indicators

Reasonable model evaluation indicators can quantify the performance of classification models, mainly including recall, precision (also known as precision rate), accuracy, and F_1-score.

(1) *Recall*

$$Recall = \frac{TP}{TP + FN} \quad (1)$$

(2) *Precision*

$$Precision = \frac{TP}{TP + FP} \quad (2)$$

(3) *Accuracy*

$$Accuracy = \frac{TN + TP}{TP + FN + FP + TN} \quad (3)$$

(4) *F1-score*

$$F_1 - score = \frac{2Recall \cdot Precision}{Recall + Precision} \tag{4}$$

where *TP*, *FP*, *FN*, and *TN* can be obtained from the confusion matrix of the classification results given in Table 1.

(5) Kruskal–Wallis test

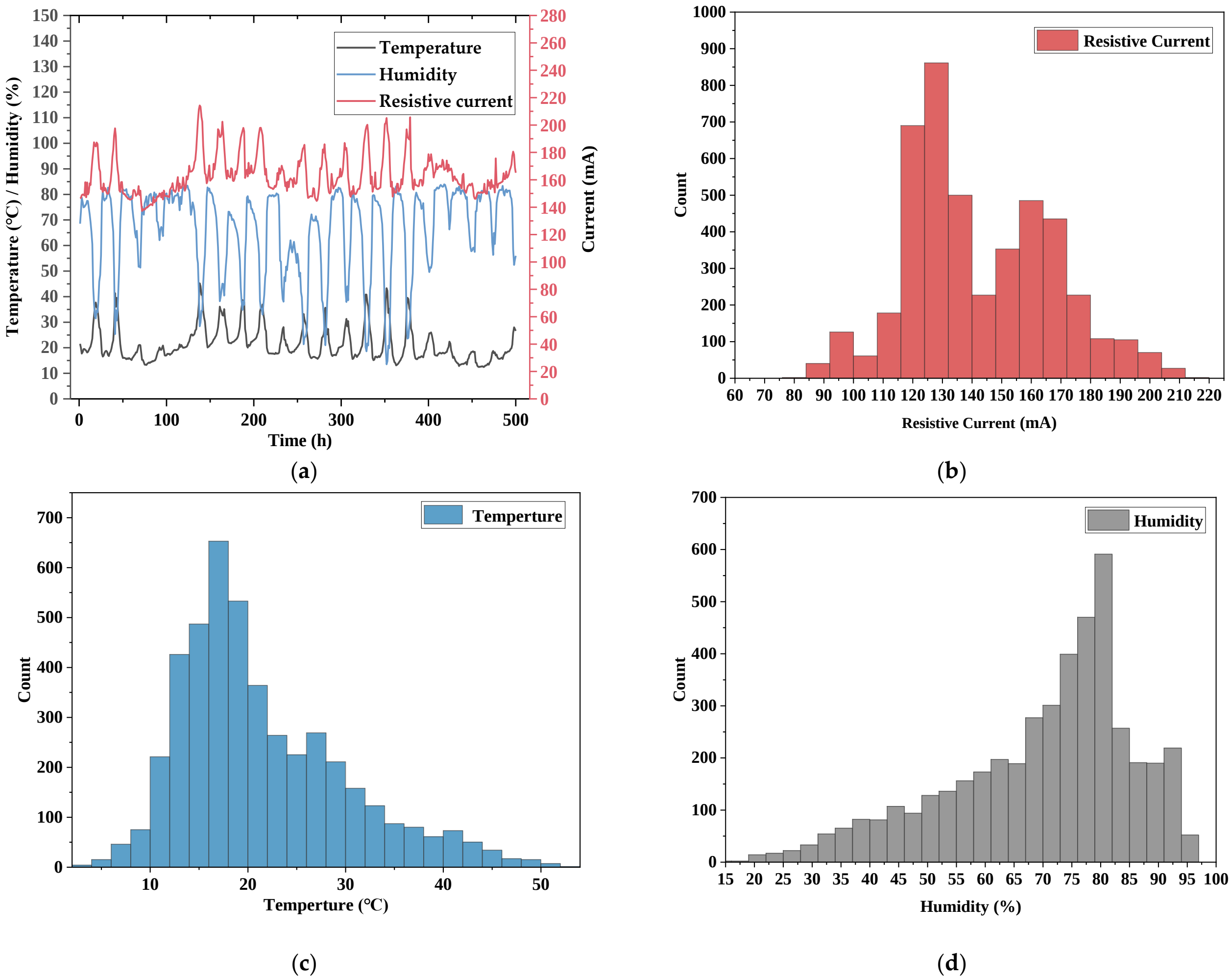

Figure 6. Original data and histograms of the frequency distribution under MOA fault condition. (**a**) Original data in respect of resistive current and environmental temperature and humidity; (**b**) histogram of the frequency distribution of the MOA resistive current; (**c**) histogram of the frequency distribution of environmental temperature; (**d**) histogram of the frequency distribution of environmental humidity under normal conditions.

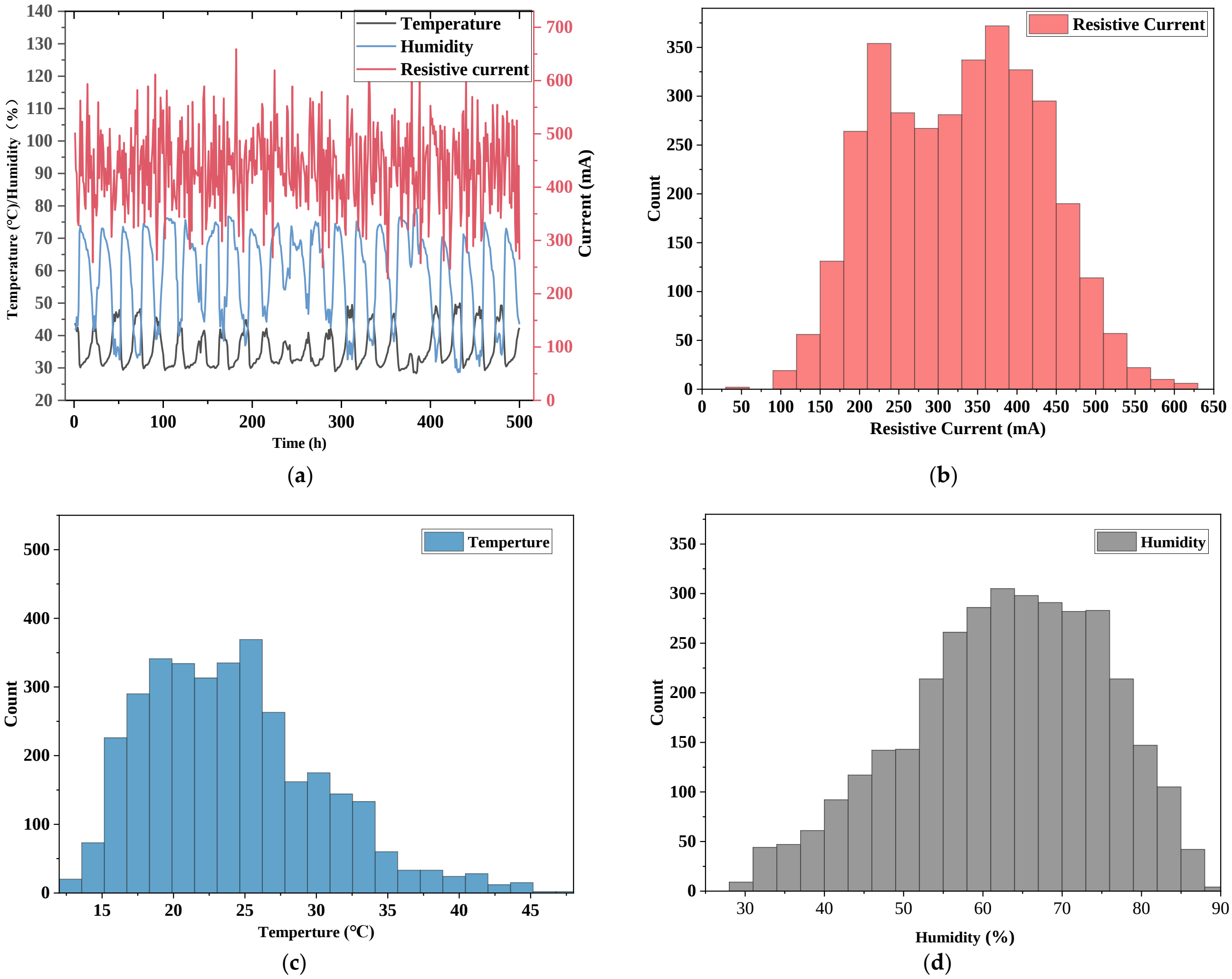

Figure 7. Original data and histograms in respect of the frequency distribution under MOA monitoring device failure conditions. (**a**) Original data regarding resistive current and environmental temperature and humidity; (**b**) histogram of the frequency distribution of the MOA resistive current; (**c**) histogram of the frequency distribution of environmental temperature; (**d**) histogram of the frequency distribution of environmental humidity under normal conditions.

Table 1. Confusion matrix for the evaluation of performance.

Reality	Prediction	
	Positive Class	Negative Class
Positive class	*TP*	*FN*
Negative class	*FP*	*TN*

The Kruskal–Wallis test was developed based on the Wilcox rank-sum test to test whether the medians are all the same between different subgroups. The original hypothesis is H_0: $M_1 = M_2 = \ldots = M_k$, where k is the number of subgroups and M_i is the overall median of the sample in group i. If the original hypothesis is rejected, this means that the medians of the k groups are not all the same, and the samples of the k groups do not all come from a single population. The Kruskal–Wallis test is a non-parametric test based on rank and does not require the original distribution of the samples.

The Kruskal–Wallis-constructed statistic is as follows:

$$H = \frac{12}{C(C-1)} \sum_{i=0}^{M} \frac{R_i^2}{n_i} - 3(C+1) \quad (5)$$

3.3. Comparison of Results before and after Suppression of Environmental Temperature and Humidity Interference

To mitigate the effects of environmental temperature and humidity on the MOA resistive current, we employ a technique for suppressing temperature and humidity disturbances using weighted nonlinear function modeling, which converts the resistive current under different environmental temperatures and humidities into the resistive current under the same reference temperature and humidity, thereby reducing the false alarm state of the MOA.

We introduce the Pearson correlation coefficient, a widely utilized measure in the field of natural sciences, to gauge the level of correlation between variable A and variable B, with a value ranging between -1 and 1. The calculation of the Pearson correlation coefficient is achieved as follows:

$$\rho_{A,B} = \frac{E(AB) - E(A)E(B)}{\sqrt{E(A^2) - (E(A))^2}\sqrt{E(B^2) - (E(B))^2}} \quad (6)$$

Table 2 shows the corresponding values of the Pearson correlation.

Table 2. Strengths of correlation for different Pearson coefficients.

Correlation	No Correlation	Weak Correlation	Moderate Correlation	Strong Correlation	Extremely Strong Correlation
Numerical value	0.0–0.2	0.2–0.4	0.4–0.6	0.6–0.8	0.8–1.0

Figure 8 shows the fluctuation in the MOA resistance current and environmental temperature and humidity monitoring data before and after suppression of the temperature and humidity interference. Table 3 shows the Pearson correlation coefficient between temperature and humidity interference before and after suppression and the environmental temperature and humidity.

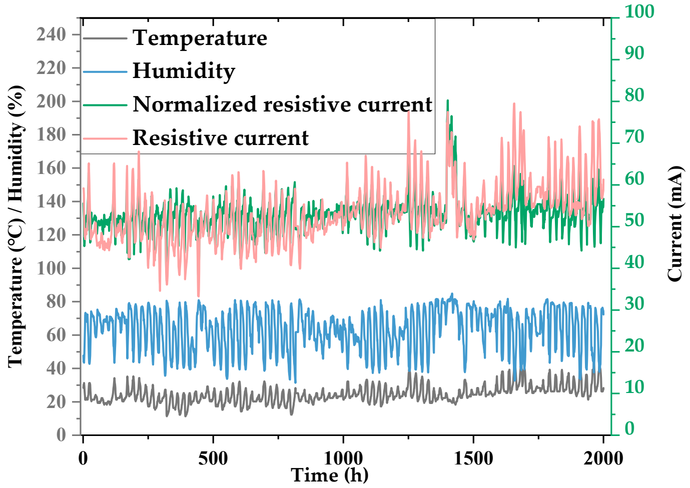

Figure 8. Fluctuation diagram of MOA resistance current and environmental temperature and humidity monitoring data before and after suppression of the temperature and humidity interference.

Table 3. Pearson correlation coefficient between MOA resistive current and environmental temperature and humidity before and after suppression of the temperature and humidity interference.

	Ambient Temperature	**Ambient Humidity**
Resistive current	0.796960	0.434868
Resistive current after temperature and humidity interference suppression	0.026346	0.001883

Figure 8 demonstrates that, prior to temperature and humidity interference suppression, the MOA resistive current shows a strong correlation with the temperature range and a moderate correlation with environmental humidity. The online monitoring of MOA resistive current is significantly impacted by changes in ambient temperature and humidity levels. The resistive current of the MOA over a longer period shows some correlation with environmental temperature and humidity after mitigating the effects of environmental temperature and humidity interference. Moreover, the fluctuation in resistive current has been significantly reduced in comparison to the pre-interference condition. The findings demonstrate that the technique for mitigating environmental temperature and humidity interference using weighted non-linear function modeling significantly diminishes the association between the resistive current and environmental factors. This ultimately decreases the impact of environmental temperature and humidity on MOA resistive current, effectively reducing erroneous warning signals due to environmental temperature and humidity influences on MOAs.

3.4. MOA Classification Algorithm Combining Suppressing Environmental Temperature and Humidity Interference with SAE

In this section, the states of the MOA are classified using an MOA classification algorithm that combines the suppression of environmental temperature and humidity interference with an SAE. In order to obtain an MOA dataset under different conditions, 80% of the data was used for training and 20% was used for testing. There are a total of 117 sets of data in the test set, including 79 sets of normal MOA data, 22 sets of primary MOA equipment fault data, and 16 sets of MOA monitoring device faults. To objectively estimate the classification ability of the algorithm, we took the average accuracy obtained from 50 runs as the measurement indicator of accuracy. We drew the confusion matrix, accuracy, and loss values of the verification set of the MOA fault identification method combining suppression of environmental temperature and humidity interference and an SAE as shown in Figure 9. Among these values, 0 indicates the normal operation state; 1 represents the MOA fault; and 2 indicates the MOA monitoring device failure.

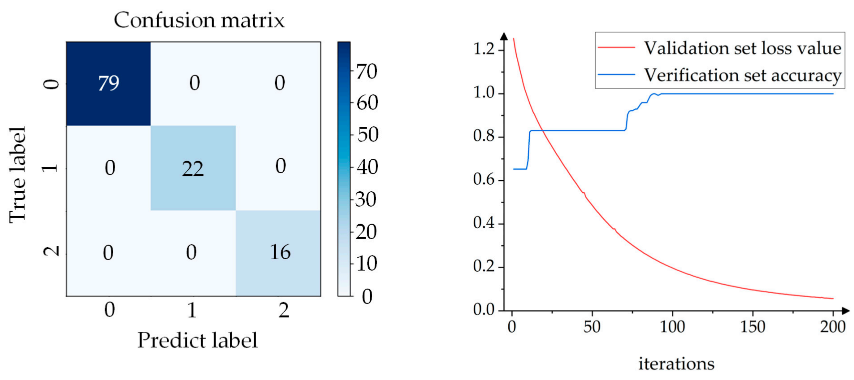

(**a**) (**b**)

Figure 9. (**a**) Confusion matrix of the MOA classification algorithm combining suppression of environmental temperature and humidity interference with SAE; (**b**) accuracy and loss values of the validation set.

3.5. Algorithm Comparison

In this section, the classification results, *recall*, *accuracy*, F_1-*score*, and *average accuracy* in respect of the SAE, random forest (RF), SVM, and logistic regression (LR) classification algorithms are compared under different conditions. Figure 10 shows the confusion matrix of four fault classification algorithms under different scenarios. Among them, ① represents using traditional classification algorithms; ② represents the use of feature fusion algorithms based on traditional classification algorithms; and ③ represents the use of a fault classification algorithm based on temperature and humidity suppression. Table 4 describes the independent samples Kruskal–Wallis test parameters for the accuracy of different classification algorithms under 50 trials. Figure 11 depicts the accuracy distribution of different MOA fault classification algorithms under 50 trials. Table 5 shows the comparison of *recall*, *accuracy*, F_1-*score*, *average accuracy*, and computation time of four fault classification algorithms under different conditions. The computer used in this study was a LAPTOP-1A84DTOQ, the system type was a x64-based PC, and the processor was an Intel64 Family 6 Model 142 Stepping 10 GenuineIntel~1792 MHz.

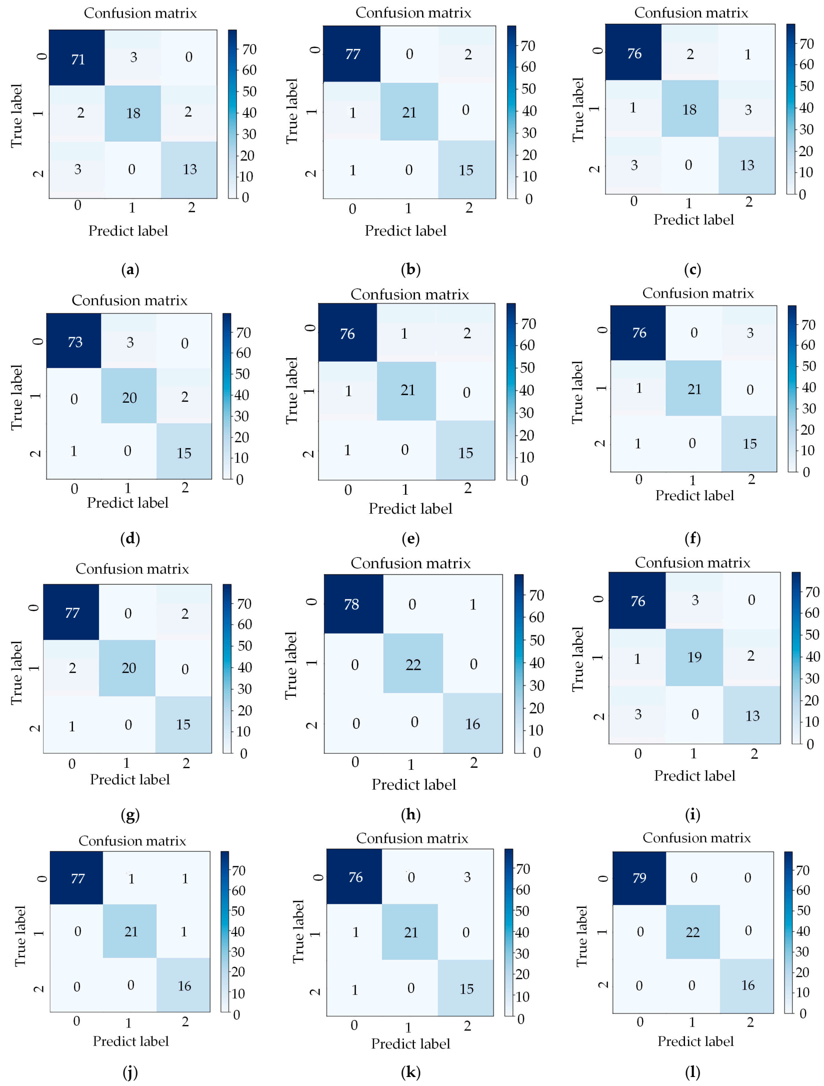

Figure 10. (**a**) Confusion matrix for SVM-based MOA fault classification algorithm; (**b**) confusion matrix for RF-based MOA fault classification algorithm; (**c**) confusion matrix for LR-based MOA fault classification algorithm; (**d**) confusion matrix for SAE-based MOA fault classification algorithm; (**e**) confusion matrix for MOA fault classification algorithm based on combination of SVM and feature fusion;

(**f**) confusion matrix for MOA fault classification algorithm based on combination of RF and feature fusion; (**g**) confusion matrix for MOA fault classification algorithm based on combination of LR and feature fusion; (**h**) confusion matrix for MOA fault classification algorithm based on combination of SAE and feature fusion; (**i**) confusion matrix for MOA fault classification algorithm based on combination of environmental temperature and humidity suppression and SVM; (**j**) confusion matrix for MOA fault classification algorithm based on combination of environmental temperature and humidity suppression and RF; (**k**) confusion matrix for MOA fault classification algorithm based on combination of environmental temperature and humidity suppression and LR; (**l**) confusion matrix for MOA fault classification algorithm based on combination of environmental temperature and humidity suppression and SAE.

Table 4. Independent samples Kruskal–Wallis test.

Sample 1 − Sample 2	Inspection Statistics	Standard Test Statistics	Significance
SAE + ③ − SVM + ①	444.98	12.83	0.00
SAE + ③ − SVM + ②	302.62	8.72	0.00
SAE + ③ − SVM + ③	155.04	4.47	8.00×10^{-6}
SA E+ ③ − LR + ①	−441.02	−12.72	0.00
SAE + ③ − LR + ②	−217.62	−6.27	3.45×10^{-10}
SAE + ③ − LR + ③	−141.34	−4.07	4.68×10^{-6}
SAE + ③ − RF + ①	−349.38	−10.07	0.00
SAE + ③ − RF + ②	−299.44	−8.63	0.00
SAE + ③ − RF + ③	−264.08	−7.61	2.59×10^{-14}
SAE + ③ − SAE + ①	−472.74	−13.63	0.00
SAE + ③ − SAE + ②	−48.30	−1.39	0.04

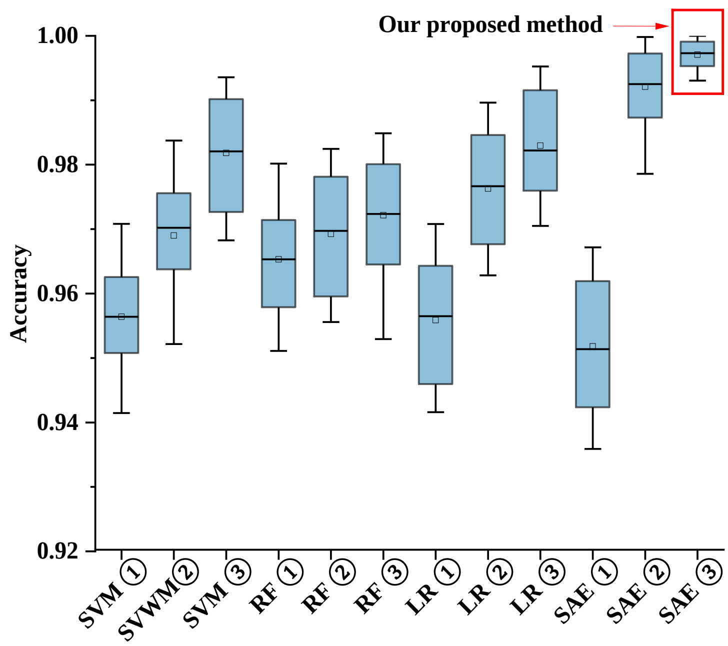

Figure 11. Accuracy distribution under 50 trials for different classification algorithms.

Table 5. Comparison of algorithm performance.

Algorithm	Method	Recall Rate	Precision	F_1-Score	Accuracy	Computation Time (s)
SVM	①	0.95783	0.95627	0.95705	0.95641	0.28492
	②	0.96832	0.96511	0.96671	0.96902	3.65214
	③	0.98101	0.98284	0.98192	0.98182	0.65291
RF	①	0.96526	0.96731	0.96629	0.96533	0.30492
	②	0.96101	0.96563	0.96331	0.96926	2.98562
	③	0.97181	0.97166	0.97173	0.97215	0.59254
LR	①	0.95818	0.95861	0.95991	0.95588	0.21456
	②	0.97209	0.97558	0.97383	0.97629	3.98756
	③	0.98187	0.98421	0.98304	0.98295	0.62135
SAE	①	0.94048	0.93103	0.93573	0.95181	0.31892
	②	0.98532	0.99101	0.98815	0.99209	5.53882
	③	0.99856	0.98621	0.99234	0.99709	0.52849

As can be seen from Figure 10, the four MOA fault classification algorithms are prone to generating false alarms in situation ①, and the normal running MOA is judged as a fault state. Compared to situation ①, the false alarm phenomenon in situation ② is reduced, but it still occurs occasionally. Compared to situation ① and situation ②, the number of false alarms in situation ③ is greatly reduced, and the SAE classification algorithm based on temperature and humidity suppression has the highest accuracy in MOA state classification.

As can be seen from Table 4, the Kruskal–Wallis test on the accuracy of different classification algorithms under 50 trials shows that the significance of the MOA fault classification algorithm combining ambient temperature and humidity interference suppression and an SAE with other classification algorithms is less than 0.05, which indicates that the accuracies of the different MOA fault classification algorithms are independent samples, and that there is a significant difference in the results for the various classification algorithms.

Figure 11 depicts the accuracy distribution of different MOA fault classification algorithms under 50 trials, and it can be seen that the fault classification algorithm combining ambient temperature and humidity interference suppression with an SAE has a high accuracy rate and a small fluctuation range compared to other MOA fault classification algorithms.

Table 5 shows that the average accuracy of the traditional fault recognition algorithms, multi-feature fusion algorithms, and environmental temperature and humidity interference suppression algorithms based on SVM is 96.9%. The average accuracy of the traditional fault recognition algorithms, multi-feature fusion algorithms, and environmental temperature and humidity interference suppression algorithms based on RF is 97.5%. The average accuracy of the traditional fault recognition algorithms, multi-feature fusion algorithms, and environmental temperature and humidity interference suppression algorithms based on LR is 97.2%. The average accuracy of the traditional fault recognition algorithms, multi-feature fusion algorithms, and environmental temperature and humidity interference suppression algorithms based on SAE is 98.1%. Comparing the training effects of the four networks, the SAE has the best fault recognition performance and reduces false alarms.

The F_1-score and average accuracy of the traditional MOA fault recognition algorithms SVM, random forest, LR, and SAE are 95.4% and 95.7%, respectively. The F_1-score and average accuracy of the MOA multi-feature fusion classification algorithm based on traditional classification algorithms are 96.7% and 97.7%, respectively. The F_1-score and average accuracy of the MOA fault recognition algorithm combining temperature and humidity interference suppression with traditional classification algorithms are 98.2% and 98.4%, respectively. This indicates that considering environmental temperature and humidity can effectively improve the accuracy and F_1-score of the MOA classification when using the same data. The combination of environmental temperature and humidity suppression with classification algorithms can significantly reduce computation time compared to algorithms combined with feature fusion. Compared to algorithms that fuse features, suppressing interference from environmental temperature and humidity on MOA resistive current can effectively mitigate the impact of environmental temperature and humidity on MOA resistive current. This can reduce false alarms and improve the identification of MOA faults.

4. Conclusions

To solve false alarm problems caused by the effect of external environmental conditions on the MOA resistive current, a method of suppressing environmental temperature and humidity interference was proposed, and a fault identification method for a metal oxide arrester combining the suppression of environmental temperature and humidity interference with an autoencoder was proposed. The conclusions are as follows:

(1) The accuracies of the different classification algorithms follow independent distributions with large variations, and the proposed MOA fault identification method, which combines environmental temperature and humidity interference suppression with an SAE, has an average accuracy of 99.7%.
(2) The average accuracy of the fault recognition algorithm based on an SAE increased by 1.2%, 0.6%, and 0.9% compared to the values for the fault recognition algorithms based on SVM, RF, and LR, respectively.
(3) Compared to traditional MOA fault recognition algorithms only considering the resistive current, the average accuracy of the MOA fault recognition algorithm with multi-feature fusion of the resistive current, environmental temperature, and humidity increased by 2%, and the proposed MOA fault recognition algorithm suppressing the interference of environmental temperature and humidity on resistive current increased by 3.7%.

Due to the lack of data samples in respect of internal moisture, aging, and superficial pollution of the MOA, the MOA failure classification algorithm that combines ambient temperature and humidity interference suppression with an SAE can only identify MOA faults and monitoring device failures from the normal state so far. In the future, we will collect more data samples of MOA faults to verify the effectiveness of the proposed method to identify the internal moisture, aging, and superficial pollution faults of the MOA.

Author Contributions: Conceptualization, S.S.; Methodology, X.Z.; Software, X.Z. and Y.R.; Validation, G.W.; Formal analysis, X.Z. and J.Z.; Investigation, Y.R.; Resources, G.W. and J.Z.; Data curation, G.W., J.Z. and Y.R.; Writing—original draft, X.Z.; Writing—review & editing, S.S.; Supervision, S.S.; Project administration, S.S.; Funding acquisition, S.S. All authors have read and agreed to the published version of the manuscript.

Funding: This work was supported by the National Natural Science Foundation of China (No. 52207150).

Data Availability Statement: Data are contained within the article.

Conflicts of Interest: Authors G.W., J.Z. and Y.R. were employed by the company State Grid Fujian Electric Power Co., Ltd. The remaining authors declare that the research was conducted in the absence of any commercial or financial relationships that could be construed as a potential conflict of interest.

Nomenclature

I_r	Resistive current
I_{r0}	Truth value of resistive current
I_r'	Corrected value of resistive current
ΔI_r	Difference between truth value and corrected value of resistive current
b	Fitting coefficient

t	Temperature
h	Relative humidity
N	Number of data samples
K	Maximum number of iterations
k	Number of iterations at termination
ε	Threshold of iterative convergence
u	Standardized residual indicator
q	Weight value
G	Fitting surface
$\boldsymbol{W_1}$	Encoder weight
$\boldsymbol{W_2}$	Decoder weight
$\boldsymbol{a_1}$	Encoder offset
$\boldsymbol{a_2}$	Decoder offset
$\boldsymbol{x_1}$	Input vector of SAE
$\boldsymbol{x_2}$	Feature parameter obtained from the first encoder
$\boldsymbol{x_3}$	Feature parameter obtained from the second encoder
$\boldsymbol{y_1}$	Feature parameter obtained from the first decoder
f_e	Activate function of encoder
f_d	Activate function of decoder
ρ	Pearson correlation coefficient
E	Mathematical expectation
A	Variable to be analyzed
B	Variable to be analyzed
H	Kruskal–Wallis test coefficient
n	Value of samples
M	Number of samples
R	Sum of the rank of all the samples
C	Sum of the value of samples

References

1. Ranjbar, B.; Darvishi, A.; Dashti, R.; Shaker, H.R. A survey of diagnostic and condition monitoring of metal oxide surge arrester in the power distribution network. *Energies* **2022**, *15*, 8091. [CrossRef]
2. Christodoulou, C.A.; Vita, V.; Mladenov, V.; Ekonomou, L. On the computation of the voltage distribution along the non-linear resistor of gapless metal oxide surge arresters. *Energies* **2018**, *11*, 3046. [CrossRef]
3. Christodoulou, C.A.; Ekonomou, L.; Fotis, G.P.; Gonos, I.F.; Sathopulos, I.A. Assessment of surge arrester failure rate and application studies in Hellenic high voltage transmission lines. *Electr. Power Syst. Res.* **2010**, *80*, 176–183. [CrossRef]
4. Chen, Y.; Shu, S.; Wu, H.; Wang, G.; Chen, C. Inverse distance weighted improved KNN algorithm for defect diagnosis of MOA. *J. Fuzhou Univ. (Nat. Sci. Ed.)* **2022**, *50*, 635–641.
5. Ma, Z.; Ruan, J.; Gan, Y.; Zhang, C.; Wang, J.; Du, Z. Research on resistive current calculation method of MOA based on RC network. *High Volt. Appar.* **2019**, *55*, 47–53+61.
6. Luo, T.; Hu, W.; Liu, K. On-line measurement of metal oxide surge arrester based on harmonic analysis method. *Electr. Switchg.* **2011**, *49*, 34–36.
7. Zhang, J. Application of infrared temperature measurement technology to live detection of zinc oxide arrester. *High Volt. Appar.* **2015**, *51*, 200–204.
8. Liu, H.; Li, H.; Cao, Z.; Ding, Z.; Zhao, X. Arrester fault diagnosis based on resistive current detection and infrared thermal imaging technology. *Insul. Surge Arresters* **2016**, *139*, 75–78.
9. Wei, S.; Deng, W.; Lei, H.; Mao, W.; Shi, Z.; Liu, W. Study on fault simulation and defect detection of 500 kV MOA. *Insul. Surge Arresters* **2019**, *142*, 109–114.
10. Cao, H.; Yang, Z.; Hua, R.; Yang, H.; Ren, J. Study on algorithm of resistive current of MOA. *High Volt. Appar.* **2015**, *51*, 32–36.
11. Dobrić, G.; Žarković, M. Fuzzy expert system for metal-oxide surge arrester condition monitoring. *Electr. Eng.* **2021**, *103*, 91–101. [CrossRef]
12. Zhou, A.; Song, H.; Fang, Y.; Chang, Z. Fault diagnosis of MOVA based on evidence theory. *Appl. Mech. Mater.* **2014**, *556*, 2685–2688. [CrossRef]
13. Huang, S.; Hsieh, C.H. A method to enhance the predictive maintenance of ZnO arresters in energy systems. *Int. J. Electr. Power Energy Syst.* **2014**, *62*, 183–188. [CrossRef]
14. Bassi, W.; Tatizawa, H. Early prediction of surge arrester failures by dielectric characterization. *IEEE Electr. Insul. Mag.* **2016**, *32*, 35–42. [CrossRef]

15. Wei, D.; Jiang, Y.; Zhang, X.; Li, L.; Wei, Z.; Xue, F.; Li, H.; Xie, J. Comprehensive evaluation method of operation status of zinc oxide surge arrester based on information fusion. *Insul. Surge Arresters* **2019**, *142*, 68–74.
16. Zhao, Y.; Wang, Y.; Qin, P.; Zhang, J.; Li, M. Study on state evaluation of zinc oxide arrester based on fuzzy set pair analysis. *Electr. Electron.* **2020**, *40*, 28–31.
17. Li, T.; Fang, W. Research on calculation method of resistive current of metal oxide arrester based on particle swarm optimization. *Electr. Eng.* **2021**, *22*, 104–108.
18. Yang, Z.; Cao, H.; Li, P.; Cheng, Z.; Zhu, J. On-line monitoring of metal oxide arrester using genetic algorithm. *High Volt. Eng.* **2015**, *41*, 3104–3109.
19. Lira, G.R.S.; Costa, E.G. MOSA monitoring technique based on analysis of total leakage current. *IEEE Trans. Power Deliv.* **2013**, *28*, 1057–1062. [CrossRef]
20. Lira, G.R.S.; Costa, E.G.; Ferreira, T.V. Metal-oxide surge arrester monitoring and diagnosis by self-organizing maps. *Electr. Power Syst. Res.* **2014**, *108*, 315–321. [CrossRef]
21. Hoang, T.T.; Cho, M.Y.; Alam, M.N.; Vu, Q.T. A novel differential particle swarm optimization for parameter selection of support vector machines for monitoring metal-oxide surge arrester conditions. *Swarm Evol. Comput.* **2018**, *38*, 120–126. [CrossRef]
22. Khodsuz, M.; Mirzaie, M. Monitoring and identification of metal–oxide surge arrester conditions using multi-layer support vector machine. *IET Gener. Transm. Distrib.* **2015**, *9*, 2501–2508. [CrossRef]
23. Chen, C.N.; Hoang, T.T.; Cho, M.Y. Parameter optimisation of support vector machine using mutant particle swarm optimisation for diagnosis of metal-oxide surge arrester conditions. *J. Exp. Theor. Artif. Intell.* **2019**, *31*, 163–175. [CrossRef]
24. Wei, B.; Zuo, Y.; Liu, Y.; Luo, W.; Wen, K.; Deng, F. Novel MOA fault detection technology based on small sample infrared image. *Electronics* **2021**, *10*, 1748. [CrossRef]
25. Zhang, C.; Guo, Y.; Li, M. Review of development and application of artificial neural network models. *Comput. Eng. Appl.* **2021**, *57*, 57–69.
26. Ding, S.; Li, H.; Su, C.; Yu, J.; Jin, F. Evolutionary artificial neural networks: A review. *Artif. Intell. Rev.* **2013**, *39*, 251–260. [CrossRef]
27. Zhou, N.; Liao, J.; Wang, Q.; Li, C.; Li, J. Analysis and prospect of deep learning application in smart grid. *Autom. Electr. Power Syst.* **2019**, *43*, 180–191.
28. Zhang, Z.; Zhang, D.; Qiu, R. Deep reinforcement learning for power system applications: An overview. *CSEE J. Power Energy Syst.* **2019**, *6*, 213–225.
29. Ruan, Y.; Ye, X.; Deng, M.; Wang, X.; Yang, L.; Shu, Q. A new online monitoring method for MOA based on A-VMD and ASVD. *Electric Power* **2021**, *54*, 177–185.
30. Tuczek, M.N.; Bröker, M.; Hinrichsen, V.; Göhler, R. Effects of continuous operating voltage stress and AC energy injection on current sharing among parallel-connected metal–oxide resistor columns in arrester banks. *IEEE Trans. Power Deliv.* **2015**, *30*, 1331–1337. [CrossRef]
31. Yang, Z.; Chen, L.; Du, Z.; Sun, Y. Application on capacitance during the degradation of ZnO varistor. *High Volt. Eng.* **2010**, *36*, 2167–2172.
32. Huang, X.; Luo, B.; Wang, Y.; Li, X. Influence of climatic factors on on-line monitoring of MOA using grey relational analysis. *High Volt. Eng.* **2010**, *36*, 1468–1474.
33. Seyyedbarzegar, S.M.; Mirzaie, M.; Khodsuz, M. A new approach to electrical modeling of surge arrester considering temperature effect on VI characteristic. *Measurement* **2017**, *111*, 295–306. [CrossRef]
34. Xiao, S. Practicality of Online Monitoring of Substation Surge Arrester and Influence Factors of the Research and Analysis. Master's Thesis, Fuzhou University, Fuzhou, China, 2017.
35. Ding, G.; Lu, F.; Liu, Y.; Xing, L. Research of mathematical morphology in restraining interference in on-site monitoring of metal oxide surge arrester. *High Volt. Eng.* **2006**, *32*, 44–46.
36. Wang, Z. Lightning Arrester Online Monitoring System in Inner Mongolia Power Grid Operation Analysis. Master's Thesis, North China Electric Power University, Beijing, China, 2015.
37. Xu, T.; Qin, S.; Mei, G.; Zhang, B.; Li, R.; Zhang, Y. On-line monitoring and evaluation of EHV composite insulators based on leakage currents and environmental conditions. *Insul. Surge Arresters* **2014**, *137*, 6–15.
38. Zhao, D.; Xiao, R.; Si, W.; Han, Z.; Zhang, J.; Zhou, Y.; Guo, J. Influence of temperature on characteristic parameters of metal oxide surge arrester (MOA) and discussion on correction method. *Insul. Surge Arresters* **2018**, *141*, 82–87.
39. Li, H.; Liu, J.; Xu, B. The modified method of MOA on-line monitoring parameters by eliminating external environmental factors interference. *High Volt. Eng.* **2018**, *44*, 2580–2586.
40. Shi, Y.; Xue, F.; Chen, X.; Yang, L. The influence of weather on full current measurement of 110 kV ZnO arrester. *Insul. Surge Arresters* **2023**, *146*, 43–51.